Large scale particle tracing simulation for touchless potential sensing

Kaylee Champion,* Álvaro Romero-Calvo,† and Hanspeter Schaub‡

Department of Aerospace Engineering Sciences, University of Colorado Boulder, CO, 80303

Novel active sensing technologies have been recently proposed to touchlessly measure the electrostatic potential of non-cooperative objects in Geosynchronous Equatorial Orbit and cislunar space. This technology involves a servicing spacecraft that makes us of an electron beam or UV laser to excite secondary electron and photoelectron emissions. The energy of the emitted particles is then used to determine the potential of the target with respect to the servicer. However, the electric field produced by charged spacecraft with complex geometry is highly inhomogeneous. Enhanced modeling capabilities are thus required to analyze complex shapes and differentially-charged objects in scenarios of practical interest. This work expands on a SIMION-based electrostatic simulation framework that integrates the electron beam and secondary electron dynamics. To do so, spacecraft models of SSL-1300 and GOESR are implemented in fine and coarse potential arrays in SIMION. The result is a full-scale model of active potential sensing in environments in which the Debye length is larger than the separation distance between the servicer and target.

I. Introduction

T‍HE ambition to make humans a multi-planetary species is driving an increasing interest in high Earth orbit missions. Spacecraft charging, a term that describes the electric interaction between a spacecraft and its surrounding environment, exhibits distinctive features that depart from the relatively harmless Low Earth Orbits (LEO) behavior and become a source of concern for robotic and manned space exploration. Nominal Geosynchronous Equatorial Orbit (GEO) plasma is low density (0.1-1 cm^{-3}) and high-energy (up to many keV) [1], which can lead to equilibrium spacecraft potentials of tens of kilovolts [2]. While such events are relatively infrequent, appropriate countermeasures must be put in place to prevent arcing [3, 4] or unmodeled dynamic perturbations during close-proximity operations [5, 6]. However, the ability to sustain large spacecraft potentials can also be an opportunity to develop disruptive space technologies [7, 8]. Electrostatic forces acting on multi-spacecraft formations can be used to safely detumble [9] or reorbit [10–14] uncooperative targets without establishing mechanical links. Knowledge of the target potential is, however, highly desirable in most scenarios in order to develop adequate control algorithms [15].

Novel active sensing methods are currently being studied to touchlessly sense the electrostatic potential of non-cooperative objects in GEO and deep space. Such approaches make use of a positively charged servicing craft that directs an electron beam or ultraviolet (UV) laser at the object of interest so that low-energy secondary electrons [15, 16], photoelectrons [17, 18], or x-rays [19, 20] are emitted from its surface. The servicer measures the incoming signals and, knowing its own potential, infers that of the target. Each of these approaches has its own benefits and drawbacks. Secondary electron production is maximized at moderate beam energies [1] and its measurement leads to small spacecraft potential determination errors of the order of tens of V [16]. However, as illustrated in Fig. 1(a), low-energy electron beams are steered in the presence of the inhomogeneous electrostatic field generated by the servicer-target system, increasing the uncertainty of the problem [15, 21]. X-ray generation is favored by energetic particle impacts [19], which are weakly affected by the electrostatic field. Photoelectrons generated by UV lasers have been suggested as an alternative to secondary electrons that is less dependent on the electrostatic field [17, 18]. A UV laser and a high-energy electron beam may also be utilized to generate photoelectrons and x-rays simultaneously, as shown in Fig. 1(b). This would enable more accurate and robust potential estimations [22]. However, electron emission and beam trajectory uncertainties due to the inhomogeneous electric field must be addressed for any potential sensing scheme.

The basic touchless potential sensing scenario involves two spacecraft separated by tens of meters and charged up to several kilovolts in a low-density plasma. In relevant regions, such as GEO and the cislunar plasmasheet and magnetotail

---

*Graduate Research Assistant, Department of Aerospace Engineering Sciences, University of Colorado Boulder.
†Assistant Professor, Daniel Guggenheim School of Aerospace Engineering, Georgia Institute of Technology
‡Professor, Schaden Leadership Chair, Department of Aerospace Engineering Sciences, University of Colorado Boulder.

(a) Secondary electron and X-ray methods   (b) Photoelectron method
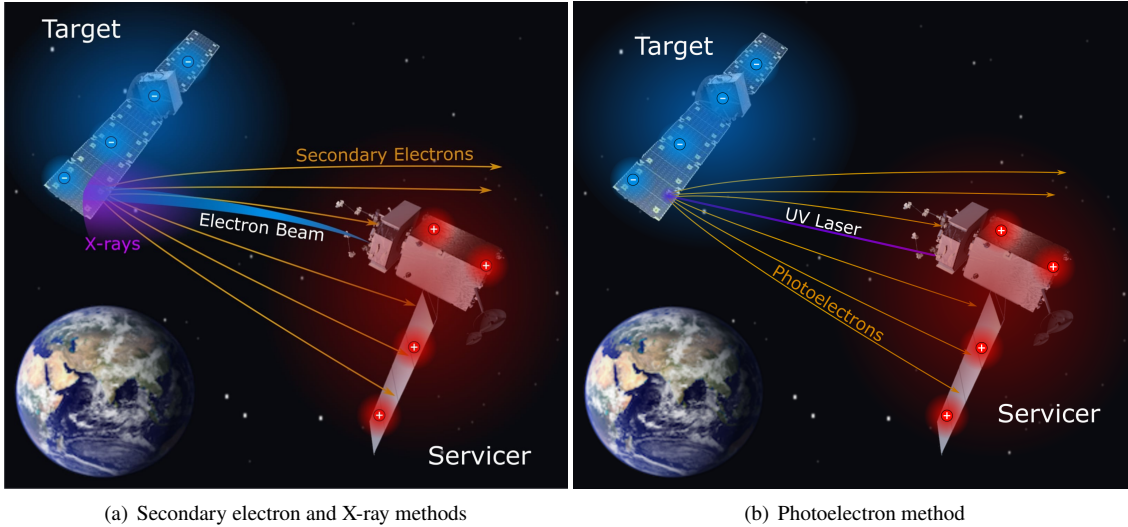
Fig. 1 By irradiating a non-cooperative target with (a) an electron beam, or (b) an ultraviolet laser, secondary electrons, photoelectrons, and x-rays are generated that enable the measurement of its electrostatic potential.

regions, space charge effects can be ignored in a first-order analysis due to the large Debye length of the environments, which can reach ~200 m [23, 24]. Although this key approximation leads to very significant computational savings by enabling a potential formulation of the electrostatic field, charged particle dynamics are still driven by the highly inhomogeneous electrostatic environment.

    Particle tracing simulations in SIMION have recently been validated for the study of the charged particle dynamics problem using vacuum chamber experiments [15] but needs to be extended to large-scale systems. Previous work does not include a nonzero servicer, which will alter the trajectories of the electron beam and electron emissions. Furthermore, a full scale model may capture dynamic charged particle behaviors that is not possible to observe on the small scale of a vacuum chamber. The full scale model will open the door to the determination of *source regions* (i.e. locations where the generation of secondaries leads to a signal measured at the servicer spacecraft [15]) within the uncooperative target object. Ultimately, the model will be utilized to develop closed-loop sensing algorithms such that a servicer may alter its position and electron beam properties to determine the potential of a target using electron emissions. In essence, this paper seeks to unlock the analysis of large-scale touchless potential sensing problems by extending a previously developed SIMION simulation framework validating the model design. Section II sets up the basic scenario and describes the physical model, and Sec. III provides validation results and preliminary characterization of sensing of a homogeneous potential target.

II. Modeling Approach

A. Electrostatic Framework

    The touchless electrostatic potential sensing model is built in SIMION by means of LUA user-defined functions [15]. SIMION computes the trajectory of each charged particle from Newton's second law

$$\frac{d\mathbf{v}}{dt} = \frac{q}{m}\mathbf{E},\tag{1}$$

where $\mathbf{v}$, q, and m are respectively the particle velocity, charge, and mass, $\mathbf{E}$ is the electric field, and t is the time. Relativistic corrections are implemented when Lorentz's factor $\gamma = \sqrt{1 - v^2/c^2}$ exceeds 10^{-10}, with c being the speed of light. The electric field is derived from the electrostatic potential field V as

$$\mathbf{E} = \nabla V,\tag{2}$$

while V is computed by solving Laplace's equation

$$\nabla^2 V = 0 \tag{3}$$

in the simulation domain. SIMION employs a regular Cartesian mesh with boundary conditions determined by set potentials of each electrode (Dirichlet) or by the zero-derivative of the potential V (Neumann). The potentials of the electrodes can be individually adjusted in SIMION, and the additive property of the Laplace equation is utilized to determine the potential field, which is saved as a *potential array* (PA). However, boundary conditions of the simulation cannot be manually imposed, which prevents the reduction of the size of the simulation domain.

It is important to note that SIMION, by default, does not solve Poisson's equation to account for space-charge effects. This implies that charge is only found on the surface of the potential arrays, and the electrostatic environment is fully determined by the arrays. This is applicable to environments in which the Debye length, or a measure of how far the electrostatic effect persists, is large compared to the computational space, as potential shielding occurring due to the ambient plasma may be neglected. Therefore, these simulations are only applicable to a GEO or similar environment where space-charge effects are negligible [6].

B. Secondary Electron Emissions

When an electron with energy greater than the work function of the surface of the material impacts a surface, secondary electrons (SEs), or secondaries, may be emitted [1]. The secondary electron trajectories emitted from the surface of the target spacecraft due to impacts from the servicer's electron beam are modeled. SIMION does not include a model for secondary electron emissions, but a user-defined LUA function has been written and validated with experimental work to expand the program's capabilities [15]. A LUA function has also been written to simulate photoelectron emissions [17], but this study focuses on the secondary electron behavior. An overview of the secondary electron implementation physics is subsequently provided, and a description of the implementation of this physics into SIMION is given in Ref. 15.

The secondary electron yield δ is the probability that a secondary electron is emitted during a primary electron impact. The yield is dependent on the incident energy E of the primary electron, and can be approximated with the Sanders and Inouye yield model [25]

$$\delta(E, 0) = c \left[e^{-E/a} - e^{-E/b} \right], \tag{4}$$

where $a = 4.3 E_{max}$, $b = 0.367 E_{max}$, and $c = 1.37 \delta_{max}$. The parameter δ_{max} is the maximum yield, and E_{max} is the energy at the maximum yield point. In this study, the spacecraft are assumed to have pure aluminum surfaces with a δ_{max} of 1.0 and E_{max} of 300 eV [26]. In reality, the surface of the spacecraft surface may be composed of different materials and will experience contamination that will change the surface properties. The yield is also dependent on the incidence angle ϕ, where $0°$ is defined for normal incidence [27]

$$\delta(E, \phi) = \delta(E, 0) e^{\beta_s (1 - \cos\phi)}, \tag{5}$$

where [1]

$$\beta_s = e^\zeta, \tag{6a}$$

$$\zeta = 0.2755(\xi - 1.658) - \left\{ [0.2755(\xi - 1.658)]^2 + 0.0228 \right\}^{1/2}, \tag{6b}$$

$$\xi = \ln (E/E_{max}). \tag{6c}$$

In order to determine the incidence angle of the primary electron, the normal direction must be defined in SIMION. This may be done in two ways, analytically and estimating from electric field. The analytic definition of the normal direction is implemented by manually defining the geometry of the system, and the particle's direction in the computational space with respect to the surface is computed upon impact. The electric field is theoretically perpendicular to the surface, so the surface normal may also be determined from the ambient electric field. This is simpler to implement, but jagged or curved surfaces may cause inaccuracies in the electric field computation. Therefore, the electric field a defined number of grid units away can be used to define the surface normal, and the averaging effect of the Laplace equation helps avoid the inaccuracies close to the surface.

The emission angle of a secondary electron is nearly independent of the angle of incidence, and the polar angle θ of the emissions can be computed from a uniformly distributed 0-1 random variable x [28, 29]

$$\theta = \frac{1}{2} \text{acos}(1 - 2x), \tag{7}$$

3

while the azimuthal angle is defined as a uniform distribution from 0° to 360°.

The emission energy E_s is on the order of a few eV and follows a characteristic distribution with a peak at one third the work function φ of the surface material. The Chung-Everhart probability distribution function [30]

$$f(E_s) = \frac{6\varphi^2 E_s}{(E_s + \varphi)^4},$$

(8)

is often used to model this. For this study, the work function of aluminum is defined as 4.20 eV [26].

C. Problem Geometry

To properly model the ambient potential field properties, the outermost external boundary is defined to be a Debye length from the spacecraft, which is ~200 m in GEO. A grounded electrode is set at the external boundary, or a Dirichlet boundary condition of 0 V is defined to simulate the decay of the electrostatic field. In order to properly define spacecraft within this computational space, elements on the order of centimeters are required. However, defining an approximately 400 m wide numerical space on the order of a few centimeters is too computationally expensive, and fields hundreds of meters away from the spacecraft do not require as high of a definition. Therefore, two sets of potential arrays with differing element sizes are utilized to efficiently represent the computational space. The internal, more finely defined PA captures the geometry of the system, while the outer, more coarse PA captures the decay of the electrostatic potential field. These PAs are defined in separate geometry (.gem) files, `SCs_eval_fine.gem` and `SCs_eval_coarse.gem`.

In the fine PA, the servicer and target are modeled after the GOES-R and SSL-1300 spacecraft, respectively, as shown in Fig. 2. The SSL-1300 model consists of a 2.5x2.5x3 m cube main body and two 12.1x2.3x0.1 m solar panels. The solar panels are shifted 0.5 in the positive z-direction away from the center of the main body. The GOES-R model consists of a 4x4x6 m main body, a 8.3x4x0.1 m solar panel, and a 8.3x0.16x0.17 m boom.

To generate the entire electrostatic field with elements on the order of a few meters, the spacecraft are defined in the coarse PA as spheres with equivalent self capacitance as the spacecraft models. The self capacitance of the spacecraft is found using the Multi-Sphere Method (MSM). The MSM uses several spheres to approximate the charge distribution of complex shapes, the servicer and target for this study [31]. The radius R_{eff} of a single sphere with equivalent capacitance C to the MSM is

$$R_{\text{eff}} = \frac{C}{4\pi\epsilon_0},$$

(9)

where ϵ_0 is the permittivity of free space. The radius of the GOES-R model is 4.44 m and the SSL-1300 model is 4.80 m, as shown in Fig. 2, and these radii values are referred to as the effective radius. The coarse elements are defined as approximately half the effective radii, or 2 meters. In addition, the electrode surface enhancement feature is utilized, which allows electrode points to be defined in partial grid units. This is particularly useful for curved surfaces, such as spheres, or rotated surfaces in which the surface does not align with the PA elements and can improve the accuracy of the potential field by at least an order of magnitude [32]. This option helps to counteract uncertainties that arise as a result of jagged surfaces and allows the spacecraft to be rotated in the computational space without loss of accuracy. This is implemented using the command `surface=fractional` in the .gem file in SIMION.

D. Potential Field Regeneration

The SIMION example `field_emission` is followed to implement a fine and coarse PA and automatically regenerate the PAs in order to represent the computational space with different PA definitions. The potential field of the entire computational space is first found using the coarse PA. In order to ensure the external boundary is 200 m from the closest spacecraft, the servicer is always located at (200,200,200) meters in the computational space. The target position relative to the servicer is defined by the user, and the external boundary is expanded such that the boundary is 200 meters from the closest spacecraft. For example, if the target is located 30 meters from the servicer in the x direction, the size of the coarse PA is 430 meters in the x direction and 400 meters in the y and z directions. Once the spheres' position and potential and the size of the PA are defined, the potential field is determined by refining the mesh. However, the problem requires that all potential arrays, in this case, the fine and coarse arrays, be present at the start of the simulation. Therefore, the finely defined model of the spacecraft is also included in the workbench and shifted such that the spacecraft are in the same position as their effective spheres, as shown in Fig. 3. The potentials of the spherical and finely defined spacecraft are also defined using a *fast adjust*. Then, the problem is regenerated, and the potential field in the coarse PA is determined and saved.
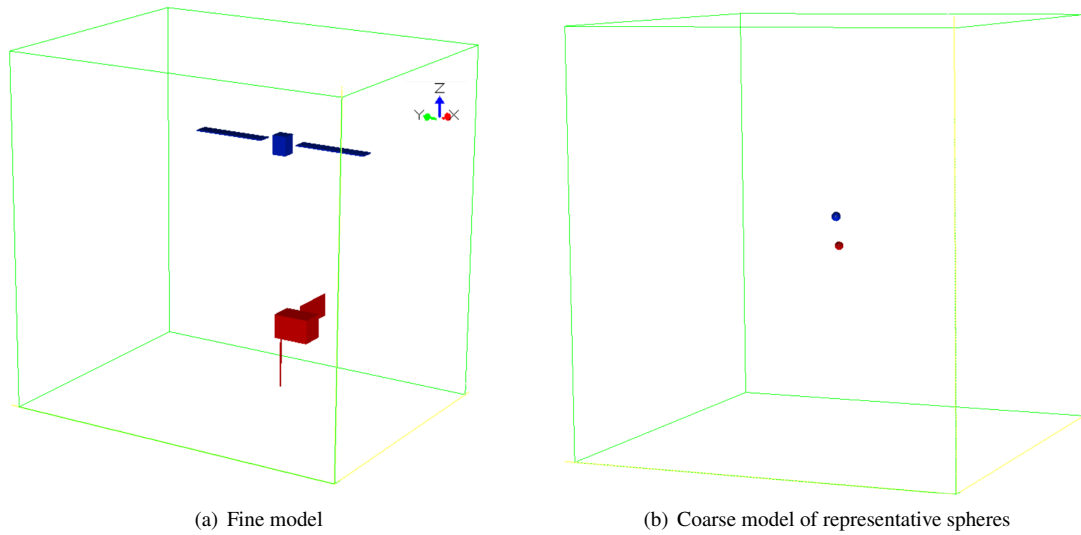
(a) Fine model

(b) Coarse model of representative spheres

Fig. 2 SIMION spacecraft fine and coarse models of servicing (red) and target (blue) spacecraft with potential field boundaries shown in green
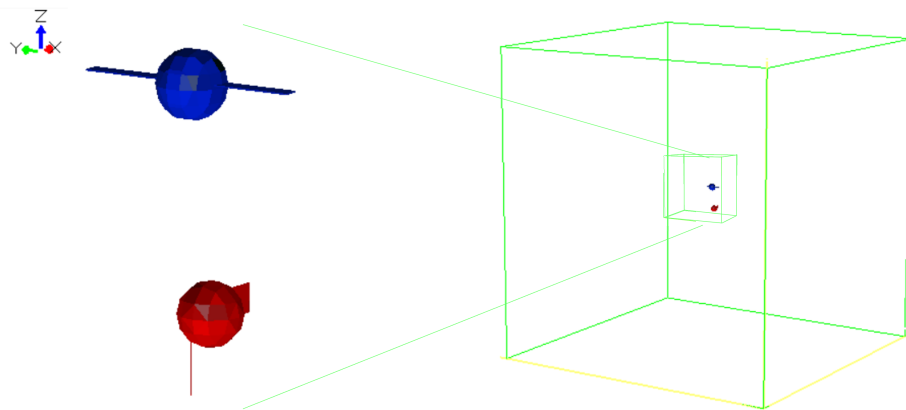

Fig. 3 SIMION spacecraft and PA boundaries for regeneration of the coarse PA

Once the potential field in the coarse PA is calculated, the potentials at the appropriate positions are transferred onto the boundary electrodes of the fine PA as Dirichlet conditions using the `refinelib.lua` function developed by David Manura in SIMION's `field emissions` example [32]. This generates a more accurate representation of the potential field in the area surrounding the spacecraft models. If multiple PAs are present in SIMION, the PA instances are listed in order from one to the number of instances. If a particle is in the presence of multiple PA it will only see the electric field defined by the PA with the highest instance number. Note that this is the PA with the highest numerical value, so if there are two PAs, the PA with instance number 2 will be prioritized. For this study, the fine PA is given priority and is defined as PA instance 2. Once the fine PA boundary conditions are defined, the effective spheres are given a potential of zero and moved to the edge of the coarse computational space so that they do not interact with the electron beam and secondary electron emissions. The area within the fine PA then resembles the example shown in Fig. 2.

The boundaries of the fine computational space also vary depending on the relative locations of the target and servicer in order to optimize the computational efficiency of the simulation. The external boundary is defined to be approximately 3 spacecraft widths from the models, as the electrostatic environment surrounding complex spacecraft shapes can be approximated with an effective sphere if the distance is larger than 2 to 3 craft radii [33, 34]. In other words, at this distance from the spacecraft models, the imposed Dirichlet boundary conditions may be considered a reasonable approximation.

MATLAB is employed to configure the PA geometry, launch the SIMION simulation, and analyze the results. The function `segment.initialize_run()` is employed to automatically regenerate the PAs as defined and fly the electron gun particles. Particle collisions are detected using the `segment.terminate()` function, and if the particle's final position is within defined boundaries, the final position, velocity, and kinetic energy is printed. MATLAB achieves this through the use of a Window's batch file and commands defined in Appendix M of [32].

E. Space Environment

Considerations of the space environment's influence on touchless potential sensing in GEO is presented in Ref. 15. Primary concerns are detectability of secondaries with respect to the ambient environment, collisions, and particle interactions with the magnetic field. GEO plasma is low density (0.1-1cm^{-3}) and high energy, up to several keV. Therefore, the mean free path is on the order of 100 AU, which is orders of magnitude larger than potential sensing separation distances, and the plasma may be considered collisionless. Reference 35 shows that the magnetic field influence on particle trajectories in GEO is a secondary effect compared to the spacecrafts' electrostatic field influence and thus is neglected in this study. Furthermore, the flux of secondary electrons is orders of magnitude larger than the ambient environment flux [35].

III. Preliminary Results

A. Computational Assessment

An assessment of the computational efficiency and accuracy of the simulation is presented. First, the efficiency of the computation with 10 cm element sizes and 20 cm element sizes in the fine PA and 2 m elements in the coarse PA is compared. For this comparison, there is a separation distance of 30 meters between the servicer and target, and the target is positioned such that the electron beam emitted by the servicer impacts the main body. The target is given a potential of -2500 V, the servicer 0 V, and the electron beam an energy of 5 keV with a half angle of 1°. 100 particles are flown, and the number of secondary electron emissions that impact the side of the servicer's main body facing the target is recorded. The secondary electron trajectories appear to be consistent between tests, as shown in Fig. 4, and 20 particles and 19 particles are detected for the 10 cm element and 20 cm element sizes, respectively. Furthermore, the computation takes approximately 1.5 hours with 10 cm element sizes and 5 minutes for 20 cm element sizes. Therefore, the fine PA is defined with 20 cm elements.

The trajectory solutions are also compared to previous secondary electron simulations conducted using the MSM in Ref. 21. In this scenario, the target is again -2500 V, the servicer is 0 V, the separation distance is 30 m, the beam energy is 5 keV, and the beam half angle is 1°. The relative positions are also defined such that the electron beam hits the target's solar panel. For comparison, the PAs are determined using the process outlined in Section II.D and using only the fine PA with Neumann boundary conditions of zero, as shown in Fig. 5. The range of secondary electron emission angles is wider in the MSM simulation as the SEs are uniformly distributed within the electron beam impact area, while the emission angles in SIMION are defined using Eq. 7. However, the SE trajectories for similar emission

(a) Fine PA with 10 cm elements   (b) Fine PA with 20 cm elements
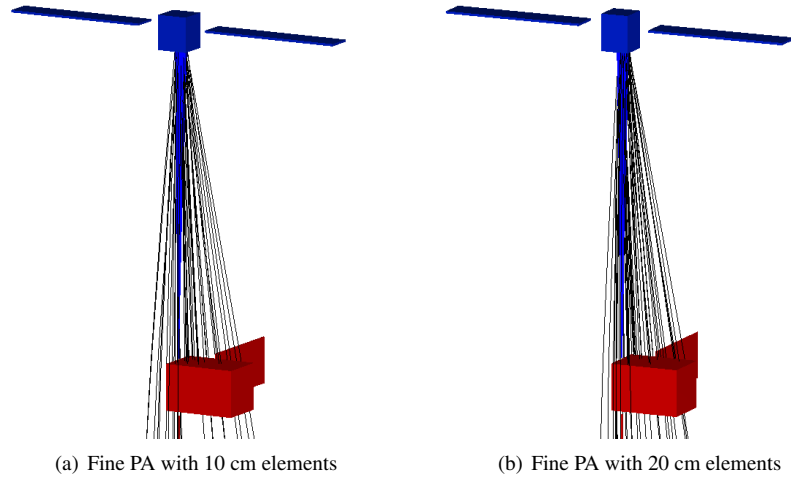
Fig. 4   Secondary electron trajectories (black) emitted from a -2500 V target by an electron beam (blue) in a fine PA with varying element resolution.

Table 1   Sensing for homogeneous servicer and target potentials analysis parameters

Parameter	Value
Beam energy, E_B	5000 eV
Initial divergence angle, δ	1 deg
Initial beam radius, r_B	1 mm
Number of particles, n	100
Servicer potential, V_{serv}	0 V
Target potential, V_{tar}	-500, -1500, -2500, -3500 V
Target angle about the x-axis, α	0° - 180°
Separation distance	30 m

angles may be compared. The SIMION trajectories when the fine PA is regenerated based on the coarse PA field closely resembles the MSM results. The SIMION trajectories without this refinement differ significantly from the MSM. The electron beam does not fully impact the solar panel, and the SE emissions are deflected significantly more towards than servicer. This validates the SIMION PA determination method and exemplifies the importance of accurately defining the boundary conditions.

B. Target potential and angle variation

The ultimate aim of this study is to characterize the positions at which the secondary emissions are detectable for a range of target potentials and position with respect to the servicer. To do so, the potential of the target is given a range of potentials from -500 V to -3,500 V in 500 volt steps, and the target is rotated about the x-axis in 1 degree steps from 0° to 180°. The servicer and target are separated by 30 meters, and the target is positioned such that the electron beam impacts the center of the main body at 0°. This is the same relative position as shown in Fig. 4, and the characterizing parameters are shown in Table 1. The normal direction with respect to the target surface is determined using the electric field direction one grid unit away from the surface, and jagged surfaces are accounted for through the use of the `surface=fractional` command in SIMION. This study aims to characterize regions in which the target's SEs may impact the servicer, so any particle that impacts the side of the servicer closest to the target is detected and extracted for analysis. In servicing scenarios, the energy of the particles is measured using an RPA, which is typically a few centimeters in diameter. As a result, the placement of the RPA and size will limit the regions in which the secondary electron emissions are detectable, and the optimal placement and size of the RPA is a subject of future work.

(a) MSM SE trajectories [21]

(b) SE trajectories after full regeneration of PAs

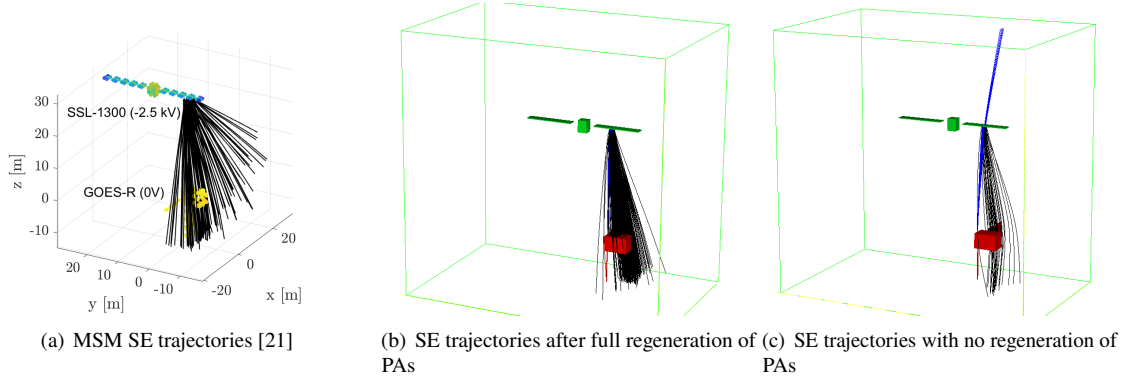(c) SE trajectories with no regeneration of PAs

Fig. 5 Secondary electron trajectories (black) emitted from a 2500 V target by an electron beam (blue). The left figure shows the trajectories defined using the MSM [21], the middle figure shows trajectories when the process defined in Section II.D is used to refine the PAs, and the right figure is shown when only the fine PA and Neumann boundaries conditions are used to define the PA.
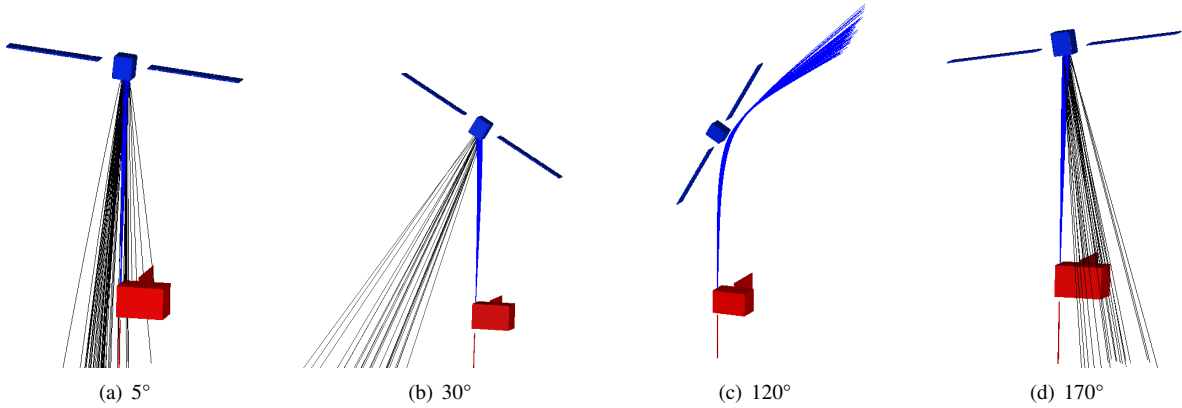

(a) 5° (b) 30° (c) 120° (d) 170°

Fig. 6   Electron beam (blue) and secondary electron (black) trajectories for different -2500 V target angles α

1. Overview of secondary electron trajectories

There are three possible scenarios that occur while detecting the electron emissions from a target as shown in Fig. 6 for a -2500 V target: the beam is deflect and does not impact the target (α=120°), the beam impacts the target but the secondaries are not detected (α=30°), and the beam impacts the target and secondaries are detected (α=5°, 170°). These regimes have been presented in previous works but the studies were not full scale and have not included the presence of a servicer [15, 36].

The described regimes will exist for most target potentials, but the angles at which the target is detectable is dependent on several variables, including the target potential. As the potential of the target changes, the deflection of the electron beam changes, resulting in a different area of the target being impacted. This phenomenon is shown in Fig. 7, as the target potential is varied from -500 V to -3500 V and the angle is held at 120°. The electron beam clearly experiences more deflection as the target potential increases, and below -2500 V the beam not longer impacts the target.

C. Detectability Analysis

This set of simulations aims to show at which servicer position with respect to the target the secondaries are detectable. Rotating the target about the x-axis simulates a servicer traveling in a circle about the target in order to measure its potential. Figure 8 plots the resulting number of particles detected versus angle for each target potential. The target is detectable from approximately 0° to 50 ° and 150° to 180°. Outside this range, the beam either does not hit the target or does not generate secondaries with trajectories that impact the servicer. Thus, the optimal angles at which
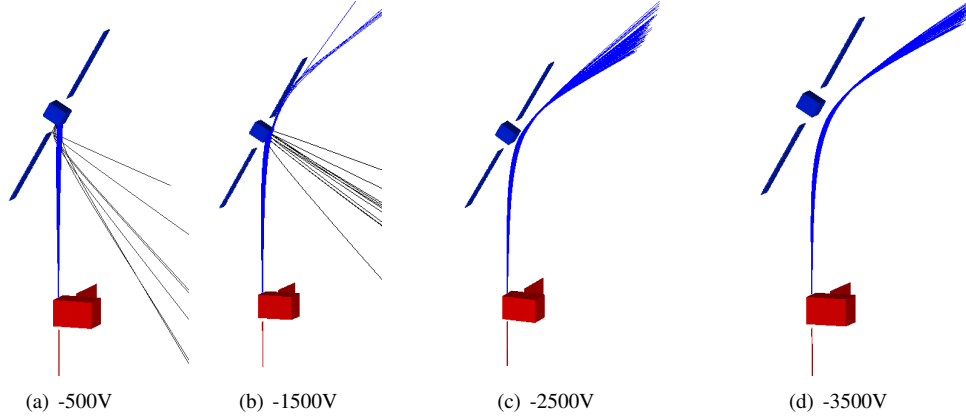
(a) -500V   (b) -1500V   (c) -2500V   (d) -3500V

Fig. 7   Electron beam (blue) and secondary electron (black) trajectories for target angle at $\alpha=120°$
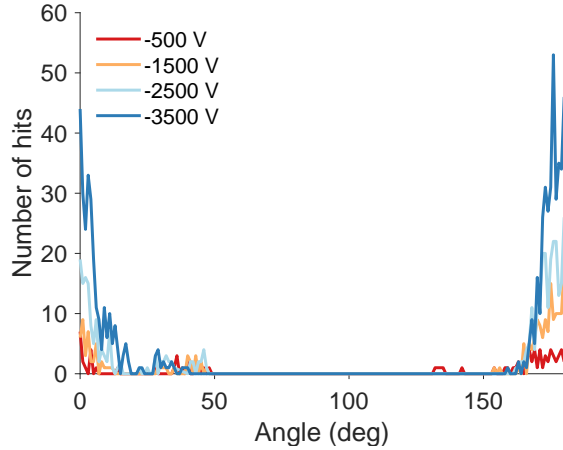

Fig. 8   Number of SE particle impacts on the servicer versus target angle about the x-axis

the target is detectable is as close to a normal incidence angle as possible. However, this may not be feasible during in-situ potential sensing, as the target may be rotating or may have a complex shape without an obvious flat surface to detect the potential. As a result, this SIMION model may be utilized to approximate the *source regions* of the target, or the regions in which electron emissions from the target may be detected. Furthermore, control algorithms may be developed using this SIMION model in order to make potential sensing using electrons more robust, as the servicer may adjust its position or electron beam properties in-situ in order to optimize detection of emissions.

The asymmetry in the results is due to the shift of the solar panels of the target, as described in Sec. II.C. An example of this is shown in Fig. 9, as the target is rotated such that it is 45° from a normal incidence angle (0° and 180°). The location of the solar panels with respect to the target has a distinguishable impact on the electron beam impact location, as the potential field close to the target is altered. This exemplifies the need to create representative models of the electrodes in touchless potential sensing models, as geometrical errors may have unexpected impacts on the source regions. This also emphasises the need for control algorithms, as the surface properties of the spacecraft are likely altered in space, or there may be errors in the SIMION representation of the spacecraft. Thus, the servicer must be capable of adjusting in-situ to these complications.

The number of particles detected also increases as the potential of the target increases. This is likely the result of implementing a high energy electron beam, as the arrival energy E_{eff} of the beam is

$$E_{\text{eff}} = E_B + q_e V_{\text{tar}} - q_e V_{\text{serv}} \quad \text{for } q_e V_{\text{serv}} - q_e V_{\text{tar}} < E_B, \tag{10a}$$

$$E_{\text{eff}} = 0 \quad \text{for } q_e V_{\text{serv}} - q_e V_{\text{tar}} \geq E_B, \tag{10b}$$
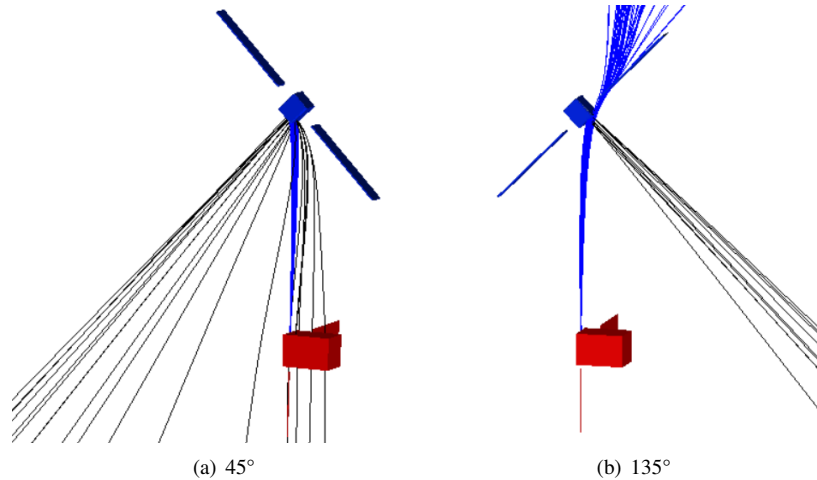
9

(a) 45°   (b) 135°

Fig. 9 Electron beam (blue) and secondary electron (black) trajectories for target potential at -2500V and angle 45° from normal

where q_e is the elementary charge. In other words, as the target becomes more negative, the arrival energy of the beam decreases. As stated in Section II.B, the energy at which the secondary electron yield is highest is 300 eV. Therefore, as the arrival energy of the beam decreases, the energy approaches 300 eV and the yield increases. This demonstrates the importance of selecting an appropriate beam energy, as higher energy beams experience less deflection due to the electrostatic environment. However, if the target energy is low, a high energy beam may not be optimal for secondary emissions. Therefore, the beam energy must be selected such that the yield is sufficiently high, but the beam is not significantly deflected. This problem may also be countered through the use of UV lasers, and future models in SIMION will include UV laser and photoemissions to explore this.

IV. Conclusion

This work expands the SIMION electrostatic framework presented in Ref. 15 to simulate touchless potential sensing using electron emissions on the full scale. The efficiency of the computation is optimized using a coarse and fine PA, and the results are validated with previous simulations using the Multi-Sphere model. Simulations to determine the source regions at which the target is detectable show that the optimal detection position is close to a normal incidence angle, and the problem is sensitive to asymmetries in the target spacecraft. Future work will involve implementing photoemissions into the model and utilizing the results to develop control algorithms that enable a servicer to determine the regions in which the electron emissions from a charged target is detectable.

Acknowledgments

References

[1] Lai, S. T., *Fundamentals of Spacecraft Charging: Spacecraft Interactions with Space Plasmas*, Princeton University Press, 2012.

[2] Olsen, R. C., "Record charging events from Applied Technology Satellite 6," *Journal of Spacecraft and Rockets*, Vol. 24, No. 4, 1987, pp. 362–366. https://doi.org/10.2514/3.25925.

[3] Roeder, J. L., and Fennell, J. F., "Differential Charging of Satellite Surface Materials," *IEEE Transactions on Plasma Science*, Vol. 37, No. 1, 2009, pp. 281–289. https://doi.org/10.1109/TPS.2008.2004765.

[4] Ferguson, D. C., Murray-Krezan, J., Barton, D. A., Dennison, J. R., and Gregory, S. A., "Feasibility of Detecting Spacecraft

Charging and Arcing by Remote Sensing," *Journal of Spacecraft and Rockets*, Vol. 51, No. 6, 2014, pp. 1907–1913. https://doi.org/10.2514/1.A32958.

[5] Wilson, K., and Schaub, H., "Impact of Electrostatic Perturbations on Proximity Operations in High Earth Orbits," *Journal of Spacecraft and Rockets*, Vol. 58, No. 5, 2021, pp. 1293–1302. https://doi.org/10.2514/1.A35039.

[6] Wilson, K., Romero-Calvo, A., and Schaub, H., "Constrained Guidance for Spacecraft Proximity Operations Under Electrostatic Perturbations," *Journal of Spacecraft and Rockets*, Vol. 59, No. 4, 2022, pp. 1304–1316. https://doi.org/10.2514/1.A35162.

[7] Romero-Calvo, A., "Novel electromagnetic space applications: low-gravity magnetohydrodynamics and electron-based touchless potential sensing," Ph.D. thesis, Aerospace Engineering Sciences Department, University of Colorado, Boulder, CO, 2022.

[8] Wilson, K. T., "Remote Electrostatic Potential Determination for Spacecraft Relative Motion Control," Ph.D. thesis, Aerospace Engineering Sciences Department, University of Colorado, Boulder, CO, 2021.

[9] Casale, F., Schaub, H., and Biggs, J. D., "Lyapunov Optimal Touchless Electrostatic Detumbling of Geostationary Debris Using Surface Multisphere Models," *AIAA Journal of Spacecraft and Rockets*, Vol. 58, No. 3, 2021. https://doi.org/10.2514/1.A34787.

[10] Schaub, H., and Moorer, D. F., "Geosynchronous Large Debris Reorbiter: Challenges and Prospects," *The Journal of the Astronautical Sciences*, Vol. 59, No. 1, 2012, pp. 161–176. https://doi.org/10.1007/s40295-013-0011-8.

[11] Hughes, J., and Schaub, H., "Prospects of Using a Pulsed Electrostatic Tractor With Nominal Geosynchronous Conditions," *IEEE Transactions on Plasma Science*, Vol. 45, No. 8, 2017, pp. 1887–1897. https://doi.org/10.1109/TPS.2017.2684621.

[12] Bengtson, M., Wilson, K., Hughes, J., and Schaub, H., "Survey of the electrostatic tractor research for reorbiting passive GEO space objects," *Astrodynamics*, Vol. 2, No. 4, 2018, pp. 291–305. https://doi.org/10.1007/s42064-018-0030-0.

[13] Hughes, J. A., and Schaub, H., "Electrostatic Tractor Analysis Using a Measured Flux Model," *Journal of Spacecraft and Rockets*, Vol. 57, No. 2, 2020, pp. 207–216. https://doi.org/10.2514/1.A34359.

[14] Hammerl, J., and Schaub, H., "Effects of Electric Potential Uncertainty on Electrostatic Tractor Relative Motion Control Equilibria," *Journal of Spacecraft and Rockets*, Vol. 59, No. 2, 2022, pp. 552–562. https://doi.org/10.2514/1.A35165.

[15] Romero Calvo, Á., Hammerl, J., and Schaub, H., "Touchless Potential Sensing of Differentially Charged Spacecraft Using Secondary Electrons," *AIAA Journal of Spacecraft and Rockets*, Vol. 59, No. 5, 2022, pp. 1623–1633. https://doi.org/10.2514/1.A35355.

[16] Bengtson, M. T., Wilson, K. T., and Schaub, H., "Experimental Results of Electron Method for Remote Spacecraft Charge Sensing," *Space Weather*, Vol. 18, No. 3, 2020, pp. 1–12. https://doi.org/10.1029/2019SW002341.

[17] Romero-Calvo, A., Champion, K., and Schaub, H., "Touchless Spacecraft Potential Sensing Using Energetic Electron Beams and Active Photoemissions," *16th Spacecraft Charging Technology Conference*, 2022.

[18] Romero Calvo, Á., Champion, K., and Schaub, H., "Enabling Ultraviolet Lasers for Touchless Spacecraft Potential Sensing," *IEEE Transactions on Plasma Science*, 2023. *under review*.

[19] Wilson, K. T. H., and Schaub, H., "X-Ray Spectroscopy for Electrostatic Potential and Material Determination of Space Objects," *IEEE Transactions on Plasma Science*, Vol. 47, No. 8, 2019, pp. 3858–3866. https://doi.org/10.1109/TPS.2019.2910576.

[20] Wilson, K. T., Bengtson, M. T., and Schaub, H., "X-ray Spectroscopic Determination of Electrostatic Potential and Material Composition for Spacecraft: Experimental Results," *Space Weather*, Vol. 18, No. 4, 2020, p. e2019SW002342. https://doi.org/10.1029/2019SW002342.

[21] Romero-Calvo, A., Cano-Gómez, G., and Schaub, H., "Simulation and Uncertainty Quantification of Electron Beams in Active Spacecraft Charging Scenarios," *Journal of Spacecraft and Rockets*, Vol. 59, No. 3, 2022, pp. 739–750. https://doi.org/10.2514/1.A35190.

[22] Wilson, K., Bengtson, M., and Schaub, H., "Remote Electrostatic Potential Sensing for Proximity Operations: Comparison and Fusion of Methods," *Journal of Spacecraft and Rockets*, Vol. 59, No. 5, 2022, pp. 1425–1436. https://doi.org/10.2514/1.A35071.

[23] Seubert, C. R., Stiles, L. A., and Schaub, H., "Effective coulomb force modeling for spacecraft in earth orbit plasmas," *Advances in Space Research*, Vol. 54, No. 2, 2014, pp. 209–220. https://doi.org/10.1016/j.asr.2014.04.005.

[24] Leahy, F. B., "SLS-SPEC-159, Cross-Program Design Specification for Natural Environments (DSNE)," Tech. rep., National Aeronautics and Space Administration, 2021. URL https://ntrs.nasa.gov/api/citations/20190027643/downloads/20190027643. pdf.

[25] Sanders, N. L., and Inouye, G. T., "Secondary emission effects on spacecraft charging: Energy distribution considerations," *Spacecraft Charging Technology*, 1978, pp. 747–755. NASA-2071, ADA-084626.

[26] Lide, D. R., *CRC Handbook of Chemistry and Physics: 84th Edition*, CRC Press, 2003.

[27] Darlington, E. H., and Cosslett, V. E., "Backscattering of 0.5-10 keV electrons from solid targets," *Journal of Physics D: Applied Physics*, Vol. 5, No. 11, 1972, pp. 1969–1981. https://doi.org/10.1088/0022-3727/5/11/305.

[28] Bruining, H., *Physics and Applications of Secondary Electron Emission*, New York: McGraw-Hill Book Co., Inc. London: Pergamon Press Ltd., 1954. Chapter 7: Theory of Secondary Electron Emission; Discussion of Some Properties of Secondary Electrons.

[29] Greenwood, J., "The correct and incorrect generation of a cosine distribution of scattered particles for Monte-Carlo modelling of vacuum systems," *Vacuum*, Vol. 67, No. 2, 2002, pp. 217–222. https://doi.org/10.1016/S0042-207X(02)00173-2.

[30] Chung, M. S., and Everhart, T. E., "Simple calculation of energy distribution of low-energy secondary electrons emitted from metals under electron bombardment," *Journal of Applied Physics*, Vol. 45, No. 2, 1974, pp. 707–709. https://doi.org/10.1063/1.1663306.

[31] Stevenson, D., and Schaub, H., "Multi-Sphere Method for modeling spacecraft electrostatic forces and torques," *Advances in Space Research*, Vol. 51, No. 1, 2013, pp. 10 – 20. https://doi.org/10.1016/j.asr.2012.08.014.

[32] Manura, D., and Dahl, D., *SIMION (R) 8.1 User Manual, Rev-5*, Adaptas Solutions, LLC, Palmer, MA 01069, 2008. URL https://simion.com/info/.

[33] Schaub, H., and Jasper, L. E. Z., "Orbit Boosting Maneuvers for Two-Craft Coulomb Formations," *AIAA Journal of Guidance, Control, and Dynamics*, Vol. 36, No. 1, 2013, pp. 74–82. https://doi.org/10.2514/1.57479.

[34] Jasper, L. E., and Schaub, H., "Effective sphere modeling for electrostatic forces on a three-dimensional spacecraft shape," *AAS/AIAA Spaceflight Mechanics Meeting, Girdwood, Alaska*, 2011.

[35] Bengtson, M., Hughes, J., and Schaub, H., "Prospects and Challenges for Touchless Sensing of Spacecraft Electrostatic Potential Using Electrons," *IEEE Transactions on Plasma Science*, Vol. 47, No. 8, 2019, pp. 3673–3681. https://doi.org/10.1109/TPS.2019.2912057.

[36] Bengtson, M. T., and Schaub, H., "Electron-Based Touchless Potential Sensing of Shape Primitives and Differentially-Charged Spacecraft," *Journal of Spacecraft and Rockets*, Vol. 58, No. 6, 2021, pp. 1847–1857. https://doi.org/10.2514/1.A35086.